



Quasi-particle Interference in Sr_2RhO_4

THESIS

submitted in partial fulfillment of the
requirements for the degree of

MASTER
in
PHYSICS

| | |
|-----------------------------|----------------|
| Author : | W.O. Tromp |
| Student ID : | s1262173 |
| Supervisor : | dr. M.P. Allan |
| 2 nd corrector : | dr. W. Löffler |

Leiden, The Netherlands, August 2, 2018

Quasi-particle Interference in Sr_2RhO_4

W.O. Tromp

Huygens-Kamerlingh Onnes Laboratory, Leiden University
P.O. Box 9500, 2300 RA Leiden, The Netherlands

August 2, 2018

Abstract

The spectroscopic techniques of ARPES and spectroscopic STM play a key role in strongly correlated electron research due to their ability to resolve k -space. However, due to their different approaches in obtaining k -space information, the two techniques do not necessarily agree on the observed bandstructure. Here, in an attempt to clear the fog between the two, we present FT-STM results on the rhodate Sr_2RhO_4 focusing on the comparison between our data and previous ARPES studies on the same sample. We deduce the low-energy bandstructure through the modulations of the LDOS caused by impurity scattering. The Fermi surface area and self-energy are then calculated. We find a flattened dispersion compared to the ARPES result which is shown to be in line with previous FT-STM studies on other correlated electron materials.

Contents

| | | |
|----------|---|-----------|
| 1 | Introduction | 7 |
| 2 | Theory | 9 |
| 2.1 | Sr ₂ RhO ₄ | 9 |
| 2.2 | STM & STS | 12 |
| 2.3 | Quasi-particle Interference | 14 |
| 3 | Results | 17 |
| 3.1 | Tight-binding model of Sr ₂ RhO ₄ | 17 |
| 3.2 | STM data & Analysis | 20 |
| 3.2.1 | Cut analysis | 23 |
| 3.2.2 | Self-energy determination | 26 |
| 4 | Discussion | 29 |
| 5 | Conclusion & Outlook | 35 |
| | Appendices | 41 |
| A | Vibrations and acoustics of the UMH | 43 |

Introduction

Traditionally scanning tunnelling microscopy (STM) has been used as a technique to image the surface of samples and observe real space variations of the local density of states (LDOS) through its spectroscopic variant scanning tunnelling spectroscopy (STS). However, since the observation of Friedel oscillations in Cu(111) [1] due to scattering, STM and particularly STS has gained traction as a technique to image momentum space using Fourier Transform STM or FT-STM. Using FT-STM, the scattering vectors which give rise to the LDOS oscillations and their dispersions can be measured. From this the electronic structure of the sample can be reconstructed, albeit with the help of some necessary additional information about the bandstructure in order to disentangle the scattering vector dispersions. Due to the ever increasing stability and the superior energy resolution, FT-STM has come to rival ARPES in terms of measuring momentum space.

While in principle ARPES and FT-STM have access to the same physical information, comparing the two has proven to be less straightforward. In multiple studies discrepancies between the two have emerged. While explanations have been proposed in the form of photon polarisation on the ARPES side [2] or tunnelling elements suppressing states on the STM side [3], these proposals are specific to the cuprate under investigation in these studies. Similar discrepancies have been seen in the ruthenates with no proposed explanation to bridge STM and ARPES [4].

Here we present an FT-STM study of the rhodate Sr_2RhO_4 with the goal to map the differences between the bandstructure we observe and ARPES studies [5, 6]. From the measured dispersion of the scattering vectors we reconstruct the Fermi surface and the bandstructure, with the aid of a tight-binding model developed by Sandilands et al [7] to identify the

observed features. Having commented on the difficulties of analysing FT-STM data, we proceed to calculate the Fermi surface area of two pockets and the self-energy of one of the bands.

A comparison of our results with ARPES data reveals that the Fermi surface we obtained agrees well, while the measured dispersion is systematically flatter. Comparing the self-energies was proven to be inconclusive. A similar conclusion of an agreeing Fermi surface with a flatter dispersion is in line with an FT-STM study of the ruthenate Sr_2RuO_4 . A comment by McElroy et al [2] provides a lead to solving the discrepancy in the form of the tunnelling process through the top layer of the sample separating the Fermi liquid from the sample surface. Future calculations are needed to verify this lead.

Theory

2.1 Sr_2RhO_4

With the goal in mind to compare bandstructures as observed by ARPES and FT-STM, Sr_2RhO_4 is the ideal sample. Being a 4d transition metal oxide, Sr_2RhO_4 is closely related to the well-studied family of ruthenates. However unlike its close relative Sr_2RuO_4 , it is a paramagnetic metal down to millikelvin temperatures [8]. The absence of any low-temperature order makes Sr_2RhO_4 ideally suited to compare spectroscopic measurements.

Sr_2RhO_4 has a layered perovskite structure (figure 2.1) and is the $n = 1$ member of the Ruddlesden-Popper series $\text{Sr}_{n+1}\text{Rh}_n\text{O}_{3n+1}$. A $\sqrt{2} \times \sqrt{2}$ distortion due to rotation of the RhO_6 octahedra around the c -axis enlarges the unit cell to an in-plane lattice constant of $a = 5.44 \text{ \AA}$. Similar to the ruthenates, Sr_2RhO_4 hosts a 2D Fermi liquid in the Rh-O planes. The electronic structure of this liquid is closely related to that of Sr_2RuO_4 . However there are some key differences which can be traced back to the octahedral rotation.

Firstly, only two bands cross the Fermi level in the rhodate case, compared to three in the ruthenate case. The d_{xy} -derived γ -band from Sr_2RuO_4 is missing in Sr_2RhO_4 , leaving only the d_{xz}/d_{yz} derived α and β pockets. Calculations have shown that the octahedral rotation hybridise the d_{xy} orbital from the occupied t_{2g} states with the $d_{x^2-y^2}$ orbital from the unoccupied e_g states [9]. The formation of a bonding-antibonding pair pushes the hybridised d_{xy} states below E_F , leaving only d_{xz} and d_{yz} to cross the Fermi level.

Secondly, the enlarged $\sqrt{2} \times \sqrt{2}$ unit cell means that the Brillouin zones

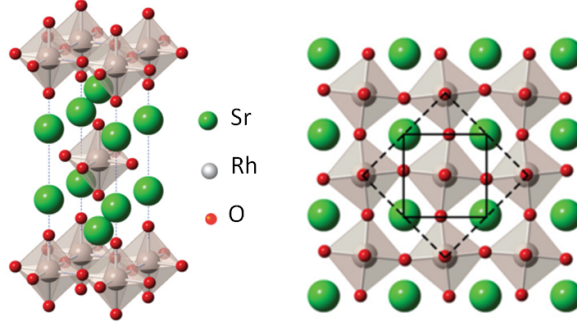


Figure 2.1: Crystal structure of Sr_2RhO_4 . The right-hand side shows the $\sqrt{2} \times \sqrt{2}$ distortion due to the octahedral rotation, with the undistorted unit cell indicated with the solid line, and the distorted unit cell with the dashed line. Image adapted from [4].

are reduced. As a result, the bands are folded inwards as shown in figure 2.2. The new, folded band structure now consists of a small α pocket and a larger β pocket centred at Γ and copies of these two bands centred at $(\pm\pi/a, \pm\pi/a)$. ARPES measurements give an average Fermi vector of $k_F \approx 0.17 \text{ \AA}^{-1}$ for the α -band and $k_F \approx 0.66 \text{ \AA}^{-1}$ for the β -band and a slightly square shape for both [5]. The same study revealed that at the points where two β -bands cross a gap opens on the Fermi surface. Consequently, the Fermi surface consists of three enclosed areas: the hole-like α pocket centred at Γ , the electron-like, lens-shaped β_M pocket centred at M , and the hole-like β_X pocket centred at X (see figure 2.2). The full Fermi surface as measured by ARPES is shown in figure 2.2.

The band structure can be characterised by a set of parameters, including the Fermi vector, Fermi velocity and the Fermi surface pocket area. The values of these parameters obtained by ARPES are summarised in table 2.1.

| | α | β_X | β_M |
|-----------------------------|----------|-----------|-----------|
| k_F (\AA^{-1}) | 0.17 | 0.63 | 0.68 |
| v_F (eV \AA) | 0.41 | 0.56 | 0.61 |
| A (% BZ) | 6.1 | 8.1 | 7.4 |

Table 2.1: Summary of Fermi vectors and Fermi velocities for the α band and the β band in the symmetry directions, and the surface areas of the α , β_X , β_M pockets. Data from [5].

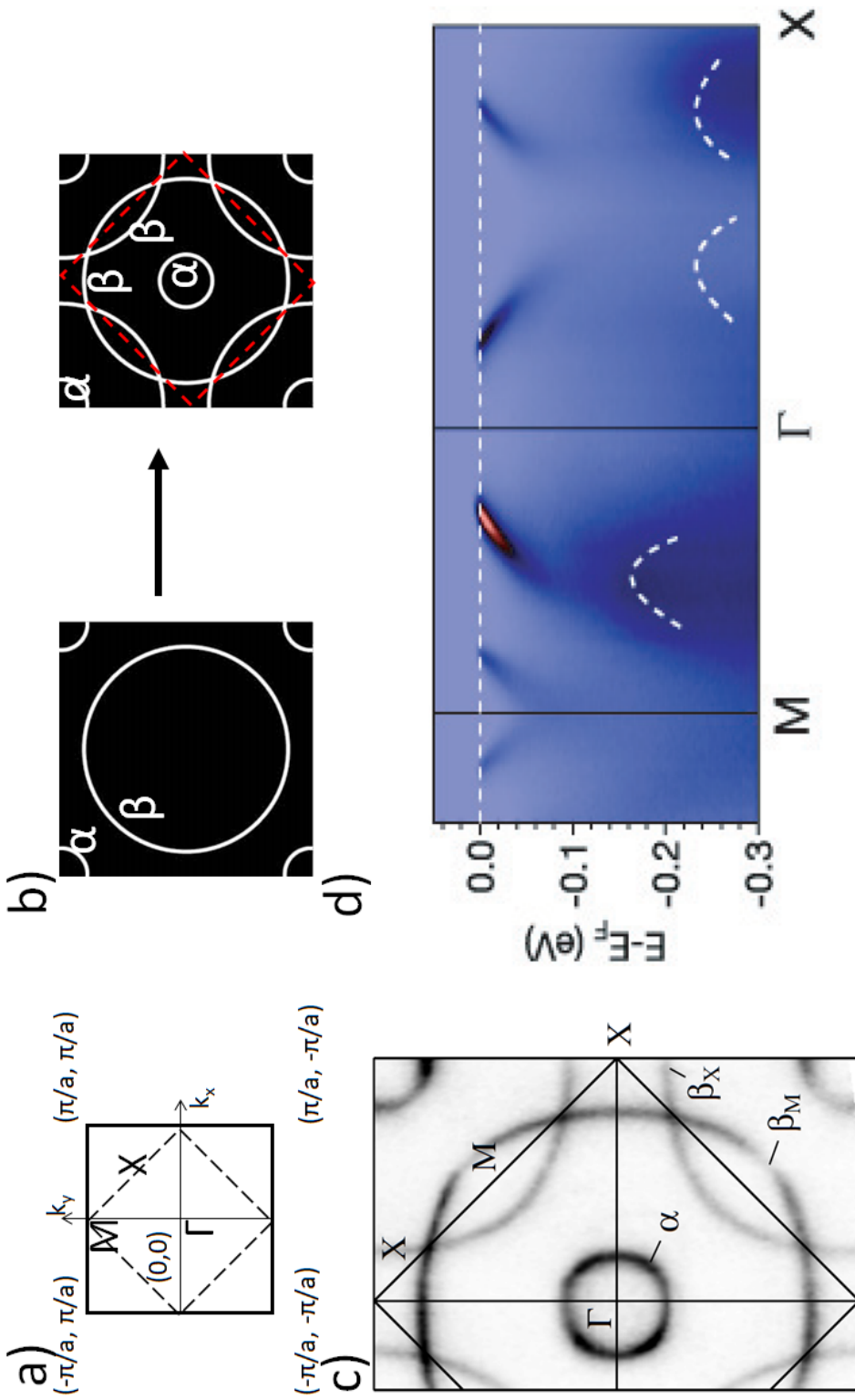


Figure 2.2: Figure a shows the effect of the octahedral rotation of the Brillouin zone, where the undistorted zone (solid line) gets reduced to the smaller distorted zone (dashed line). The high symmetry points Γ , M , X in the distorted Brillouin zone are indicated. The effect of the smaller Brillouin zone is shown in figure b where the undistorted bandstructure (left) gets folded over the new Brillouin zone boundary (red dashed lines) into the new distorted band structure (right). The α and β pockets have been approximated as circular shaped for clarity's sake. The Fermi surface as observed by ARPES [5] is shown in figure c, where now also the Fermi surface pockets α , β_M , β_X are indicated. Cuts along the high symmetry direction [6] show the dispersion of the bands and indicate where the top of the d_{xy} is predicted to be by an LDA calculation

2.2 STM & STS

The probe of choice in this study is scanning tunnelling microscopy, or STM. First demonstrated in 1982 [10], it has since become a staple in condensed matter research for its ability to image and probe the properties of a sample with atomic resolution. This is achieved by bringing a sharp metallic tip close enough to the sample surface so that, when a voltage is applied between tip and sample, a current can flow between them, without actual contact between the two. This is due to the tunnelling effect. The size of the tunnelling current is dependent of the overlap of the electron wavefunction on either side of the barrier, so it is dependent on the separation between tip and sample. Application of a bias voltage shifts the Fermi levels of the tip and sample with respect to each other, allowing electrons in occupied states on one side to tunnel to unoccupied states on the other side. The direction in which the electrons tunnel (from tip to sample or sample to tip) depends on the sign of the bias voltage. Putting this together, the tunnel current is given by [11]:

$$I = \frac{4\pi e}{\hbar} \int_{-\infty}^{\infty} [f(\epsilon - eV) - f(\epsilon)] \rho_S(\epsilon - eV) \rho_t(\epsilon) |M|^2 d\epsilon \quad (2.1)$$

with e the elementary charge, and \hbar the reduced Planck constant. The two Fermi distributions f pick out the energy window given by the bias voltage V in which tunnelling from occupied to unoccupied states occur. The density of states of the sample and tip, respectively ρ_S and ρ_t tell how many states are available in the energy window for tunnelling. The matrix element M governs the probability of the tunnelling process. In general M can be dependent on the energy ϵ , the shape of the wavefunction in the tip and sample, electron spin etc. In particular, M depends on the tip-sample distance through [12]:

$$|M|^2 \propto e^{-2\gamma}, \quad \gamma = z \sqrt{\frac{2m\phi}{\hbar^2}} \quad (2.2)$$

where z is the tip-sample distance, m the electron mass and ϕ the barrier height or work-function. Typical values for the work-function are in the 4 – 5 eV range.

Equation 2.1 can be simplified by making some assumptions. Firstly, the width of the Fermi distribution near E_F is given by $k_b T$. Meanwhile, our energy resolution is $3.7 k_b T$. Therefore we can approximate the Fermi

distributions to be step functions. Secondly, a suitable choice of tip material has a flat DOS in the energy range of a few eV around E_F . Typical tip materials W, Pt or PtIr satisfy this requirement. With these two assumptions, equation 2.1 simplifies to:

$$I = \frac{4\pi e}{\hbar} \rho_t(0) \int_0^{eV} \rho_S(\epsilon) |M|^2 d\epsilon \quad (2.3)$$

For negative bias voltages, the integration bounds would be from $-eV$ to 0. So we see that the tunnelling current is directly proportional to the integrated density of states.

During operation a feedback loop acts on the tip-sample distance to keep the current constant at some input or set-up value. Scanning the surface of a sample while in feedback will record the tip height changes needed to keep a constant current. The height changes of the tip reflect the height differences on the sample surface, essentially making an image of the surface. This type of image is called a topograph.

Relation 2.3 can be used to measure the DOS at a given bias voltage by taking the derivative:

$$\frac{dI}{dV} \propto \rho_S(\epsilon = eV) \quad (2.4)$$

STM can directly measure dI/dV , or differential conductance, by using a lock-in amplifier to modulate the bias V by a small amount dV , and measure the response dI . Doing this for a range of bias voltages gives the DOS of the sample around E_F for both the occupied and the unoccupied states. During the acquisition of the spectrum the feedback loop is switched off so that the tip height does not respond to the changes in bias voltage. This way the current change dI only reflect the DOS and do not contain extra variation due to changing tip-sample distance. One can measure the spatial variations in the DOS by measuring the dI/dV at every pixel in a field of view. To do this the feedback is switched off to collect the dI/dV spectrum, then switched on to a set-up current and bias to move the tip and record the height at the new location. This way a 3D data set called a spectroscopic map is made containing all the spectra at each pixel and the topograph. This mode of operation is called scanning tunnelling spectroscopy or STS.

2.3 Quasi-particle Interference

To compare the ARPES bandstructure with STM results, one has to relate real-space images of the local density of states (LDOS) measured by STM to the momentum-space dispersion $\epsilon(\vec{k})$ measured by ARPES. The method of choice to relate momentum-space and real-space would be the Fourier transform. To see whether this is feasible we need to relate the LDOS to some momentum-space quantity. The LDOS can be written as

$$LDOS(E, \vec{r}) \propto \sum_{\vec{k}} |\Psi_{\vec{k}}(\vec{r})|^2 \delta(E - \epsilon(\vec{k})) \quad (2.5)$$

where the wavefunction $\Psi_{\vec{k}}(\vec{r})$ contains the momentum-space information and the delta-function enforces the dispersion $\epsilon(\vec{k})$. Using a Bloch wave $\Psi_{\vec{k}}(\vec{r}) = u_{\vec{k}}(\vec{r})e^{i\vec{k}\cdot\vec{r}}$ only gives modulations through $u_{\vec{k}}(\vec{r})$, due to the fact that, by definition, the crystal momenta k diagonalise the Hamiltonian [13].

By introducing an elastic scattering centre, either an impurity or a defect, two momenta \vec{k}_1, \vec{k}_2 with $\epsilon(\vec{k}_1) = \epsilon(\vec{k}_2) = E$ now couple into each other, and as such no longer diagonalise the Hamiltonian. Instead the wavefunction becomes a linear combination of the initial and final state:

$$\begin{aligned} \Psi_E(\vec{r}) &= a_1 \Psi_{\vec{k}_1}(\vec{r}) + a_2 \Psi_{\vec{k}_2}(\vec{r}), \\ |\Psi_E(\vec{r})|^2 &= |a_1 u_{\vec{k}_1}(\vec{r})|^2 + |a_2 u_{\vec{k}_2}(\vec{r})|^2 + a_1 a_2^* u_{\vec{k}_1}^* u_{\vec{k}_2} e^{i(\vec{k}_1 - \vec{k}_2)\cdot\vec{r}} \\ &\quad + a_2 a_1^* u_{\vec{k}_2}^* u_{\vec{k}_1} e^{-i(\vec{k}_1 - \vec{k}_2)\cdot\vec{r}} \end{aligned} \quad (2.6)$$

It follows from the second line in equation 2.6 in equation 2.5, we see that the LDOS is modulated by an interference term with wavevector $\vec{q} = \vec{k}_1 - \vec{k}_2$. This modulation can be observed by STM. Specifically, the dispersion of $\vec{q}(E) = \vec{k}_1(E) - \vec{k}_2(E)$ can be obtained by performing an STS measurement over a field of view for each bias voltage $eV_b = E$ and Fourier transforming each measured energy layer to obtain $\vec{q}(E)$ for that energy value. This type of measurement is often called FT-STM.

Now we are left with two problems: what are the allowed scattering vectors and how can this be connected to ARPES data? A more detailed calculation shows that the scattering rate is approximately given by the joint density of states (JDOS), meaning the product of the DOS of the initial state and the DOS of the final state. The JDOS is given by [2]:

$$JDOS(\vec{q}, E) = \int_{\vec{k}} A(\vec{k}, E) A(\vec{k} + \vec{q}, E) d\vec{k} \quad (2.7)$$

where $A(\vec{k}, E) = \frac{1}{\pi} \text{Im}(G[\vec{k}, E])$ is the spectral function, or the imaginary part of the Green's function $G(\vec{k}, E)$. This relation allows for a relatively straightforward comparison with ARPES, by recalling that the photoemission current $I(k, E)$ is given by [14]:

$$I(\vec{k}, E) = I_0 |M_{f,i}|^2 f(E) A(\vec{k}, E) \quad (2.8)$$

where $M_{f,i}$ is a matrix element incorporating the ARPES process, $f(E)$ is the Fermi-Dirac distribution and $A(\vec{k}, E)$ is again the spectral function.

It is now clear that, barring matrix elements on both the ARPES and the STS side, the QPI pattern is given by the autocorrelation of the ARPES signal. This also reveals that the allowed scattering vectors are given by the vectors that connect parallel sections of the bandstructure at a given energy.

A crucial aspect of QPI is the fact that it is a measurement of scattering vectors, in other words a measurement of q -space, not k -space. This introduces some factors that need to be taken into account when analysing QPI pattern. Firstly, and most importantly, distances in q -space are twice as large compared to k -space. This is easy to see when considering scattering between the same band, but on opposite sides of the Brillouin zone. In that case the resulting scattering vector $q = k - (-k) = 2k$ is twice the radius of the band. This factor of two holds more generally and needs to be taken into account when deriving quantities from QPI data such as Fermi velocities and widths of bands. Secondly, only directions and sizes can be related back to k -space. All scattering vectors, no matter which parts of k -space they connect, will be translated in q -space, so that they are always start in $q = (0, 0)$. As such it is often very hard what scattering process gave rise to which scattering vector based on just a q -space map.

As a result of this second point combined with the multitude of scattering vectors that are often available, it is usually impossible to fully reconstruct the bandstructure from the QPI pattern without some additional information on what the bands are supposed to look like. As is the case in this study, this additional information is often provided by bandstructure calculations.

Results

3.1 Tight-binding model of Sr_2RhO_4

To aid in the identification of features seen in the measured QPI signal, we modelled the Sr_2RhO_4 band structure with a tight-binding model. We diagonalise the following Hamiltonian H proposed by Sandilands et al [7]:

$$H = \begin{pmatrix} H_{SO} & H_{BR} \\ H_{BR}^\dagger & H_{SO} \end{pmatrix}, \quad (3.1)$$

$$H_{SO} = \begin{pmatrix} 0 & i\lambda/2 \\ -i\lambda/2 & 0 \end{pmatrix}, \quad (3.2)$$

$$H_{BR} = \begin{pmatrix} \epsilon_{yz} & \epsilon_{rot} \\ -\epsilon_{rot} & \epsilon_{xz} \end{pmatrix} \quad (3.3)$$

The matrix H is a 4x4 matrix using two sublattices B, R to incorporate the back-folding of the band structure. Hopping to a neighbouring site is mainly through hopping between d_{yz} orbitals and between d_{xz} orbitals. These follow the dispersions ϵ_{yz} resp. ϵ_{xz} . The rotation of the RhO_6 octahedra allows for an intersite hopping term between d_{yz} and d_{xz} orbitals given by the dispersion ϵ_{rot} . The momentum dependence of these dispersions is given by:

$$\epsilon_{yz} = -2t_\delta \cos(k_x) - 2t_\pi \cos(k_y), \quad (3.4)$$

$$\epsilon_{xz} = \epsilon_{yz}, \text{ with } x \leftrightarrow y \quad (3.5)$$

$$\epsilon_{rot} = -2t_p \cos(k_x) - 2t_p \cos(k_y) \quad (3.6)$$

The presence of spin-orbit coupling mix the d-orbitals on each site. The mixing is controlled by the SO parameter λ . In summary, this model is

controlled by five parameters: three hopping terms (t_π, t_δ, t_p), a spin-orbit parameter (λ) and the Fermi level E_F . The model is evaluated by dividing the unfolded Brillouin zone into a 400x400 grid. At each of these points the dispersion relations are evaluated and the Hamiltonian H is diagonalised. The Fermi surface is then found by finding where the resulting bandstructure crosses $E = 0$. The values of the parameters are determined by optimising the model with respect to the band structure as detailed by Baumberger et al [5]. The Fermi surface from the tight-binding model and as found by ARPES are shown in figure 3.1.

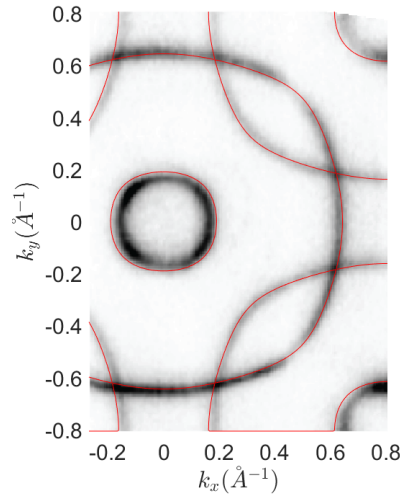


Figure 3.1: The Fermi surface as found by ARPES [5] in grey scale, with the Fermi surface from tight-binding overlaid in red lines. Along the k_x axis an artefact from the tight-binding calculation is visible in the ranges $k_x \leq -0.2$ and $0.2 \leq k_x \leq 0.6 \text{ \AA}^{-1}$.

We find that the tight-binding model is in overall good agreement with ARPES, reproducing the shape and size of the bands, although the size of the α -pocket is slightly overestimated in our calculation. This does not hinder the identification of QPI features, as we require for this purpose only good qualitative and rough quantitative agreement.

From the tight-binding contours we can generate an approximation for the DOS. We do this by finding for each energy layer E which points of the band structure fall in the window $(E - \delta E, E + \delta E)$. The use of an energy window is solely a practicality to account for floating-point errors. The DOS is then generated by putting a Lorentzian of fixed width at each point in the energy window. The resulting DOS at $E = 0$ is shown in figure 3.2a.

From the DOS at the Fermi level we already see an important feature

that can ebb through to the predicted QPI pattern. We see that the DOS on the β -band along the $(\pi/a, \pi/a)$ or the ΓM direction is relatively low. Since the QPI intensity is proportional to the DOS of both the initial and final state we can expect based on the depicted DOS that the $\beta - \beta$ scattering rate along ΓM is suppressed.

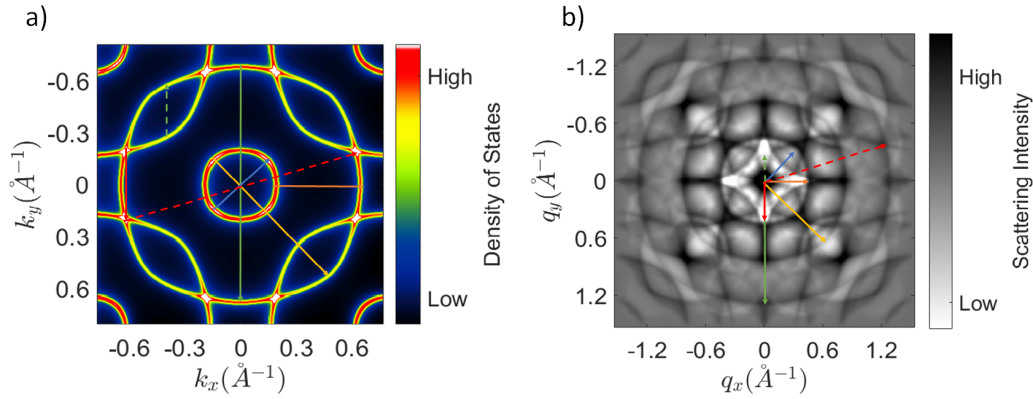


Figure 3.2: The DOS at the Fermi level (a) and the QPI pattern (b) calculated from the tight binding model. Also indicated are a set of vectors on the Fermi surface connecting regions of interest and the scattering vectors they lead to (see main text for a more detailed identification of the vectors).

A more detailed prediction of the QPI pattern can be made by taking the autocorrelation of the Fermi surface DOS, which is shown in figure 3.2b. The use of an autocorrelation as a scattering pattern implies that the scattering vectors are those that connect parallel regions on the Fermi surface. The principal of such vectors and the corresponding scattering vectors are indicated in figure 3.2 by the solid blue ($\alpha - \alpha$ scattering), solid orange ($\alpha - \beta$ scattering), solid yellow ($\alpha - \beta$ scattering) and the solid green ($\beta - \beta$ scattering) arrows. These four vectors generate four concentric circles in the QPI pattern. The rest of the scattering pattern can be understood as copies of these four concentric circles centred at $(\pm\pi/a, \pm\pi/a)$ or at $(\pm 2\pi/a, \pm 2\pi/a)$. These scattering vectors arise from scattering between bands that are not centred around the same point on the Fermi surface. An example of such a scattering is given by the dashed green arrow in figure 3.2. This vector indicates scattering between a β -band centred around $(0, 0)$ and a β -band centred around $(-\pi/a, \pi/a)$. In the scattering pattern this gives rise to a copy of $\beta - \beta$ scattering pattern (green arrow) but now centred at $(\pi/a, -\pi/a)$ or $(-\pi/a, \pi/a)$ depending on the choice on which band the initial state lies.

Note that, as mentioned in chapter 2.3, q -space is twice the size of k -space, so that q_x, q_y run from $-2\pi/a = -1.62$ to $2\pi/a = 1.62$, opposed to k_x, k_y who run from $-\pi/a = -0.81$ to $\pi/a = 0.81$. Also note that all the afore mentioned scattering vectors point from $q = (0,0)$ to somewhere in q -space, even though the underlying scattering processes are concerned with different parts of k -space.

A common interpretation of QPI data in the cuprates is that the scattering vectors are given by vectors connecting regions with high DOS [15]. This does not necessarily coincide with the interpretation of QPI scattering being an autocorrelation. This can be seen in figure 3.2 by the red arrows. Both connect regions with high DOS, however the dashed red arrow also connects parallel regions while the solid red arrow does not. As a result the calculated QPI pattern does show scattering with the dashed vector and does not show scattering with the solid vector.

3.2 STM data & Analysis

The STM data in this work were measured using a home-build STM with Nanonis electronics. Here we present two sets of STS data on the same Sr_2RhO_4 sample. A 15×15 nm topograph of the sample is shown in figure 3.3 showing some scattering centres. We also clearly observe the wavelike interference patterns centred at the scatterers. These waves are the dI/dV modulations we use to determine the dispersion. The datasets we used for analysis were taken over two different, larger field of views of 55×55 nm divided in 288×288 pixels. A lock-in modulation of 2 mV at 863 Hz. For the first data set a bias range of $[-15, 15]$ mV was used in 3 mV steps. The second data set is over a bias range of $[-50, 50]$ mV in 2 mV steps. The current setpoint for both sets was 500 pA, while the bias setpoint was -50 mV for the first set and $+50$ mV for the second set. The topographs (figure 3.3) reveal multiple scattering centres in both field of views. The cleaving plane of Sr_2RhO_4 is the Sr-O plane, so the atomic lattice visible in the topographs is the square Sr lattice. The black spots are Sr vacancies or, assuming the chemistry of Rh is similar to that of Ru, CO molecules adsorbed in a Sr vacancy [16].

The measurements were corrected for drift using the Lawler-Fujita algorithm [17]. Subsequently, the Fourier transform of the dI/dV map was taken. The resulting q -space images were symmetrised and smeared to reduce noise and ease the analysis.

The first step in analysis the QPI data is identifying what features are visible by comparing the data with the simulated QPI pattern. Shown in

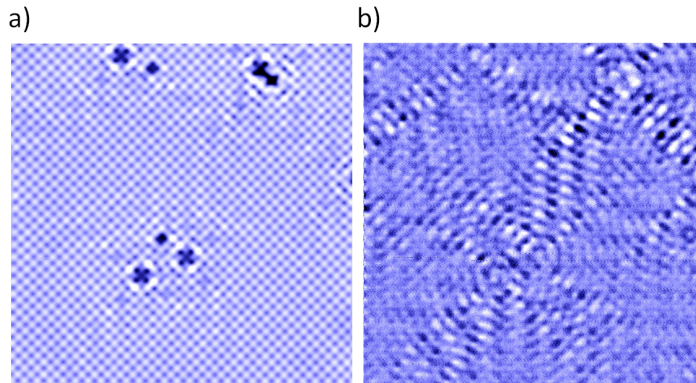


Figure 3.3: a): 15×15 nm topograph of the sample surface. The Sr atoms are clearly visible. The dark spots, most likely lattice defects act as scattering centres. b): wavelike patterns centred at the scattering centres in the dI/dV in the same field of view.

figure 3.4 are several q -space images at various energies from the two data sets. We identify the dispersing features and assign them an origin based on the modelled QPI pattern. We find four main features, identified as β band scattering (number 1 in figure 3.4, solid green line in figure 3.2), scattering between α and β band (number 2 in figure 3.4, solid orange line in figure 3.2), α band scattering (number 3 in figure 3.4, solid blue line in figure 3.2) and β scattering between two different β bands (number 4 in figure 3.4, dashed green line in figure 3.2). The bright spots in the images are the Bragg peaks (along the diagonals) and the $\sqrt{2}$ spots (horizontally and vertically oriented). The Bragg peaks are used to determine directions and distances in q -space. Please note that the images in figure 3.4 have a 45° rotated orientation relative to the QPI pattern in figure 3.2.

There are some notable differences between the measured QPI data and the predicted QPI pattern. Firstly, there are less features in the measured data. One of the most obvious missing scatterings is the second, larger scattering between the α and β band (solid yellow line in figure 3.2). Also missing are most q -vectors giving copies of the concentric shapes centred at $(\pm\pi/a, \pm\pi/a)$. Finally we see no features with high q . Presently, we cannot offer a non-speculative explanation why these bands are missing or why large q -vector scattering would be suppressed. Despite this, we are confident that the identification of features based on the modelled QPI pattern given here is correct. We do observe the decreased scattering intensity suggested by the model along ΓM for vectors 1 and 4 due to decreased DOS along the β_M pocket.

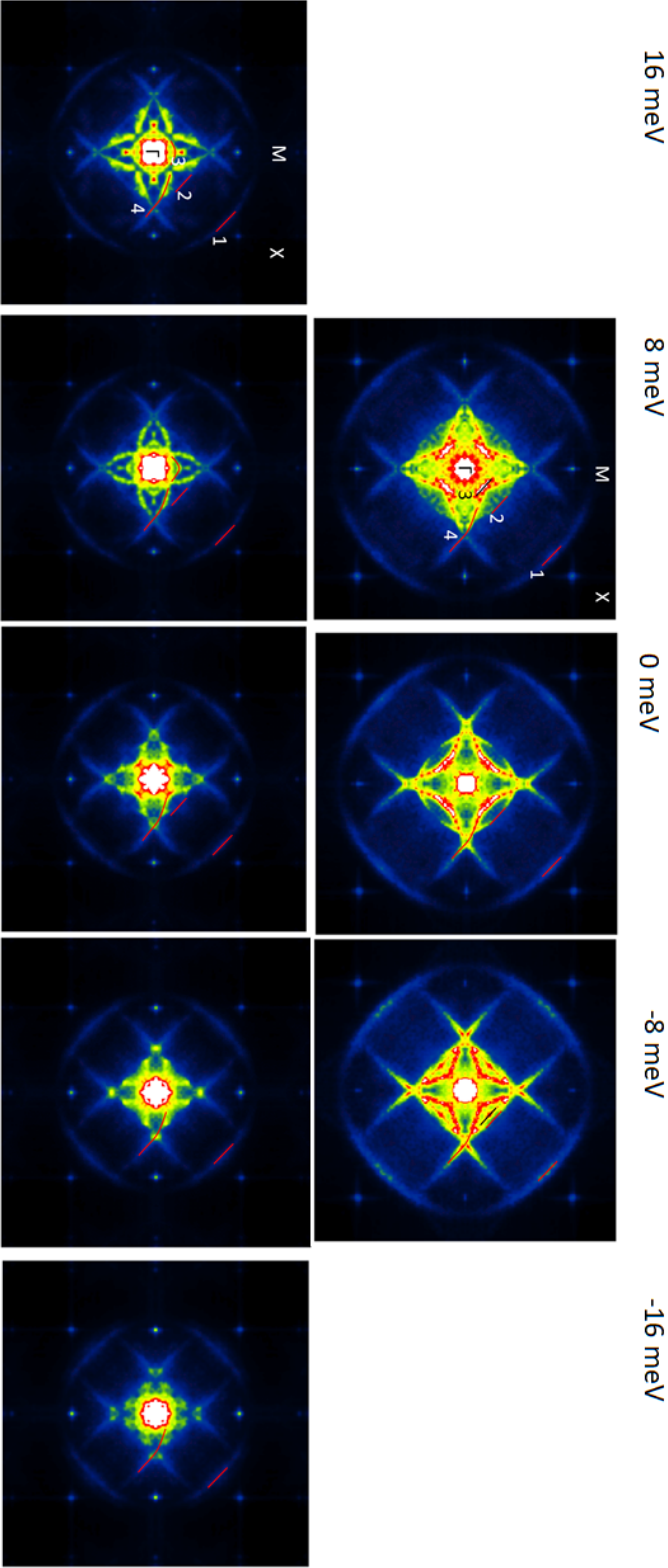


Figure 3.4: QPI patterns at various energies of the first (top row) and second (bottom row) data set. Marked and numbered are the main dispersing features identified in the main text. To ease comparison of directions in our data and ARPES data, the high symmetry directions in k -space are denoted in the q -space images by the TX and TM lines.

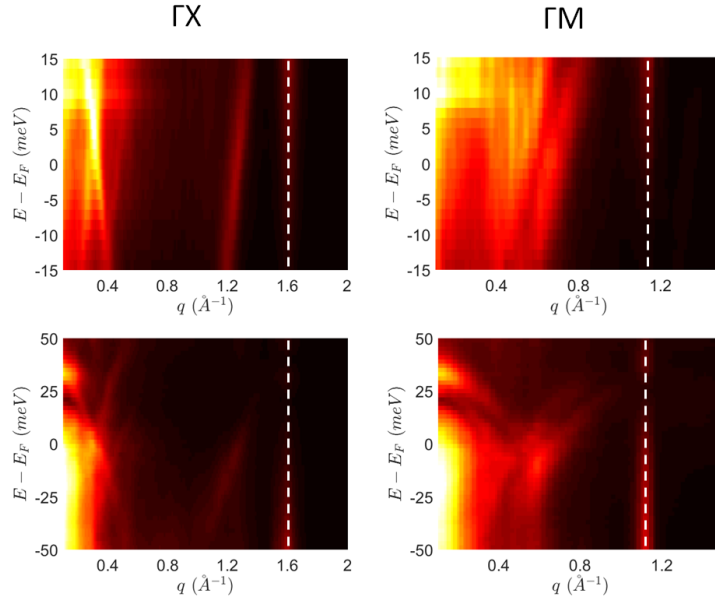


Figure 3.5: Cuts from data sets 1 (top row) and 2 (bottom row) along the high symmetry directions ΓX (left) and ΓM (right) as indicated in figure 3.4. The energy axis of the cuts from the first data set is interpolated to ease the analysis. The non-dispersive features indicated by the dashed white lines are the Bragg peaks (ΓX directions) and the $\sqrt{2}$ peaks (ΓM direction).

3.2.1 Cut analysis

To determine the underlying bandstructure, we take cuts, energy versus momentum plots, of the QPI data along the high symmetry directions ΓM and ΓX (figure 3.5). For each energy layer we fit the intensity with a Gaussian curve plus a polynomial background to determine the peak position. Fitting the peak positions as function of energy with a linear function yields the size of the q-vector and the slope of the q-vector dispersion at the Fermi level. In the case of α scattering, we use a quadratic fit through the peak position since the Fermi level is close to the top of the band. These values, together with the correct identification, gives the Fermi vectors and Fermi velocities of the bands. The resulting bandstructure parameters are summarised in table 3.1.

The fitting of the intensity curves is in general a challenging task. The reason for this is easily visible from the cuts. Given the amount of features in a QPI pattern in limited space, the observed bands generally lie close together and often cross each other. The crossings turn into an extended region with high intensity, making it difficult to fit a band close to or at the

| | α | β_X | β_M |
|-----------------------------|----------|-----------|-----------|
| k_F (\AA^{-1}) | 0.16 | 0.62 | 0.67 |
| v_F ($eV\text{\AA}$) | 0.43 | 0.43 | 0.62 |
| A (%BZ) | - | 11 | 5.8 |

Table 3.1: Summary of the Fermi vectors, Fermi velocities for the α band and the β band along the ΓX and ΓM directions, and the surface area of the closed pockets α, β_X, β_M (see figure 2.2) as a percentage of the reduced Brillouin zone. The values given here are the average over the two data sets when possible.

crossing. In such cases, and cases where the band is barely distinguishable from the background, especially the width of the curve is challenging to determine reliably, while the determination of the peak position is more robust. Examples of a close to ideal band and a more difficult case are shown in figure 3.6. The fact that the β band is far away from other features makes it relatively easy to fit (shown in figure 3.6). This fit is robust under changes of initial parameters and parameter bounds, giving reliable values for Fermi vector and velocity, and the width of the peaks. Fitting the other bands isn't so straightforward, as exemplified the fit of the $\alpha - \beta$ scattering in figure 3.6. Here, the band of interest lies in a crowded section of the cut, making the fit procedure significantly harder. As a result, fitting this band requires fine-tuning of parameters used in the fit, such as the size of the momentum window used, the maximum distance between the peaks in neighbouring energy layers and in particular the maximum width of the peaks. The fact that this last parameter plays such a role in quality of the fit severely limits the reliability of information on the width of the band. Unfortunately, most of the bands we are interested in have very similar limitations.

In principle we can reconstruct the entire Fermi surface by taking and fitting radial cuts, and extracting the Fermi vectors as function of angle with respect to k_x . Using the symmetry of the Fermi surface, only a limited range of angles is necessary. This does require that it is possible to get a reliable fit for the necessary range of angles. Regarding our measurements, this can only be done for the β scattering (number 1 in figure 3.4). This is the only band sufficiently resolved for all angles between the ΓX and ΓM lines. The other bands are either only visible for a too small range of angles or are too close to other bands to reliably fit. For the two data sets we have obtained the Fermi vector of the β band for a 90° range between two ΓX lines. The obtained positions compared to the Fermi surface from ARPES is shown in figure 3.7.

Having obtained these positions we can calculate the surface area of the two Fermi surface pockets derived from the β band, the β_M and β_X pockets. This can be done by using the symmetry of the Fermi surface giving that, for each of the pockets, the sides are equal. The values obtained for the surface areas is given in table 3.1.

While the Sr_2RhO_4 Fermi surface only has two unique bands, the QPI data shows more features than that. There is a redundancy in the dispersions we can extract from our data. This redundancy can be used to perform a self-consistency check on our analysis. For instance, take the scattering between the α and the β band. Its q -vector is given by $q_{\beta-\alpha} = k_{\beta} - k_{\alpha}$. We already know k_{α}, k_{β} from the dispersion of the β scattering and α scattering respectively. We can therefore both calculate $q_{\beta-\alpha}$

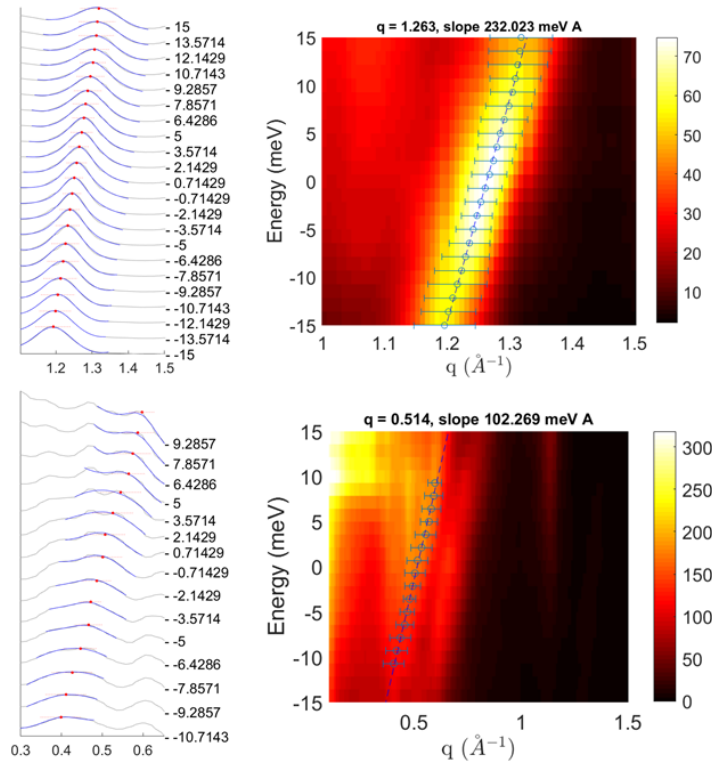


Figure 3.6: Examples of fits from which the Fermi vector and velocity is extracted. On the left are the intensity fits of each energy layer, on the right are the peak positions plotted over the cut and fitted with a linear dispersion. The latter fit gives the q -vector at $E = 0$ and the slope of the dispersion. Top row shows the fit for the β scattering in the ΓX direction, bottom row the fit for the $\beta - \alpha$ scattering in the ΓM direction.

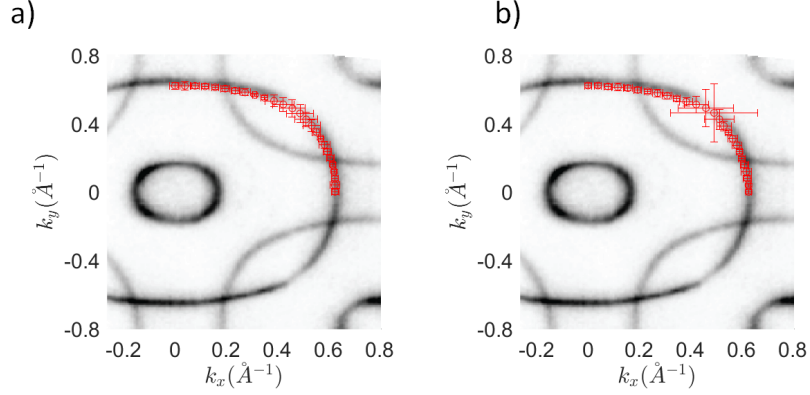


Figure 3.7: Sr₂RhO₄ Fermi surface from ARPES [5] and locations along the β band from QPI in red from the first (a) and the second (b) data set. The scattering rate along ΓM is so much suppressed in the second data set that the band cannot be reliably fit, resulting in large errorbars.

from our data, and measure it directly from the dispersion of the band we observe. If our analysis is done correctly, the two should yield similar outcomes.

The $\beta - \alpha$ scattering is observable along the ΓM direction for the first data set, and along the ΓX direction in the second set. Along ΓM we find $q_{\beta-\alpha} = 0.52 \text{ \AA}^{-1}$. Fitting the α and β bands along the same direction in the same data set yields $q_{\beta-\alpha} = 0.67 - 0.16 = 0.51 \text{ \AA}^{-1}$. Repeating this procedure for the second data set in the ΓX direction, we directly measure $q_{\beta-\alpha} = 0.44 \text{ \AA}^{-1}$ and calculate $q_{\beta-\alpha} = 0.46 \text{ \AA}^{-1}$. We find reasonable agreement between the measured and calculated q-vector for scattering between the α and β band, and conclude that our analysis is self-consistent.

3.2.2 Self-energy determination

The width of a band as measured by ARPES is related to the imaginary part of the quasi-particle self-energy, a measure for the interaction strength. The relation between the two is given by [18]:

$$FWHM = \frac{2Im[\Sigma(\omega)]}{v_F} \quad (3.7)$$

where $\Sigma(\omega)$ is the self energy, ω the energy with respect to the Fermi level, v_F the Fermi velocity and $FWHM$ is the full width half maximum

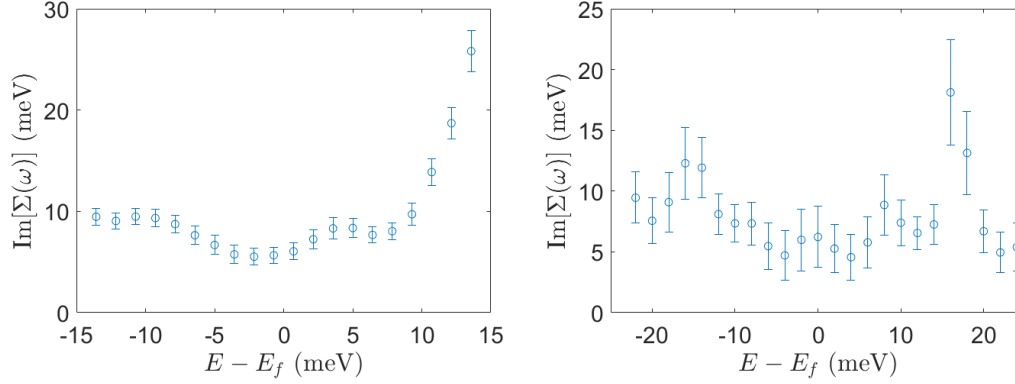


Figure 3.8: Self energies of the β band in the ΓX direction extracted from the two QPI data sets. The errorbars are given by the size of one pixel converted to an energy scale through equation 3.7

of the band. This relation uses a Lorentzian line profile at the constant energy layer ω . To use this relation for QPI data, a few adaptations need to be made. Firstly, the width measured by QPI is not the same as measured by ARPES. The QPI line shape is a convolution of the line shapes of the initial and final state. For Lorentzian curves as initial and final line shapes, the QPI curve is again a Lorentzian with a width equal to the sum of the widths of the original Lorentzians. In the case where the initial and final states originate from the same band, the QPI width is simply twice the ARPES width. Secondly, the slope of the dispersion $E(q)$ from QPI is half the slope of the dispersion $E(k)$ from ARPES, due to the differences between q -space and k -space mentioned earlier. Taking these two arguments into account, and using a Lorentzian to fit the QPI data, we can extract the self-energy.

Obtaining the self-energy does require a fit from which both the peak position and the peak width can be considered reliable. This means that we are again hindered by bands being close together or crossing each other. While peak position generally can be robustly fit, trial and error reveals that the width is only close to reliably obtained for the β scattering (number 1 in figure 3.4). However, even for this relatively easy band to fit, the width determined by the fits is sensitive to the fitting parameters, particularly the degree of the background polynomial and the size of the momentum window used. It often occurs that the fit to the first curve in the energy range yields a too high width, and only subsequent fits give a reasonable result. When calculating the self-energy we do not use the Fermi velocity v_F . However we will use the slope of the band at the energy

ω . This is the more appropriate parameter to convert between momentum and energy at said ω . We calculate this slope by doing a linear fit of the band in small window around ω . The self-energy curve obtained this way is shown in figure 3.8. The errorbars represent an error of one pixel in the width. The variation of the self energy as a result of the sensitivity to fitting parameters is roughly a few meV. The steep increase in the self energy of the small data set at positive energy is due to the determination of the peak positions at that energy. The fits at the top two energy layers gave peak positions that barely moved. For the overall Fermi velocity, which is determined by a fit through all peak positions, this doesn't matter too much as it only concerns a small fraction of the energy layer. However for the determination of the slope at those higher energy it does matter, as we can only use a small amount of energy layers. The barely changing peak positions results in a small value for the local slope, which in turn causes a steep increase in the self energy.

Discussion

The main motivation for this study is the comparison between the spectroscopic techniques FT-STM and ARPES. We provide a comparison between the STM data detailed in the previous chapter and the ARPES results reported by Baumberger et al [5] and Perry et al [6].

A first comparison is already shown in figure 3.7, where the β band obtained by QPI is shown next to the ARPES Fermi surface. The overall agreement is good, although the STM data shows a slightly more round shape and a slightly smaller Fermi vector near the ΓM line. Plotting the dispersion from QPI next to the ARPES dispersion reveals a similar picture (figure 4.1). The Fermi vectors along ΓX agree reasonably well, but along ΓM there seems to be a systematic discrepancy, with FT-STM giving the larger k_F . Note that to match the ARPES data along ΓM , the STM data points are folded back, so that a smaller k_F in figure 3.7 gives a larger k_F in figure 4.1. The full dispersions reveal that the α band from QPI matches that from ARPES well. Along ΓM the STM α band is somewhat displaced, but the k -dependence is very similar to the ARPES α band. Along ΓX the ARPES band is well reproduced from the second data set, and reasonably well reproduced by the first data set for low energy. At higher energy, where some discrepancy emerges, the dispersion from the first data set is extrapolated.

The dispersion of the β band is reproduced less well, consistently having a smaller slope. This is the case for both the energy range where our data is extrapolated (higher energies for the first data set) and for energy ranges we have access to in our data (low energy for the first data set, full energy range for second set).

The comparison of the self energies (figure 4.2) is less informative for a number of reasons. First, there is the intrinsic uncertainty in our deter-

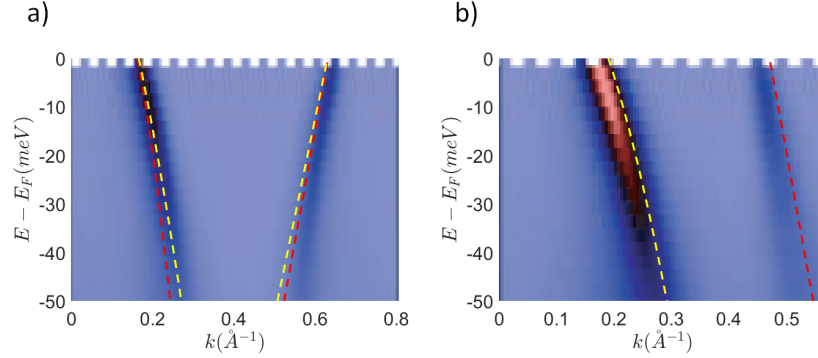


Figure 4.1: The fits through the bands observed in the QPI pattern plotted over the dispersion measured by ARPES [6] along the ΓX (a) and the ΓM (b) directions. The dashed red line shows the bands from the first data set and is extrapolated to cover the $-50 - 0$ meV energy range. The dashed yellow line shows the bands from the second data set, where no extrapolation is needed. For both directions, $k = 0$ lies in the Γ point.

mination of the self-energy as discussed before. Secondly, we have only managed to obtain the self-energy for the β band, while only the α self-energy is acquired from ARPES. Lacking any information on the nature of the dominant interactions in Sr_2RhO_4 , it is unreasonable to expect the self-energy to be equal across the various bands. The only comparison to make is the magnitude of the self-energy, which is roughly equal.

The determination of the self-energy from especially the second set suffers from an additional problem in the form of a non-dispersing artefact figure 4.3. At low energies, being so close to the band, the artefact interferes with the intensity fits, further complicating the determination of the peak widths. The presence of a non-dispersing artefact in STS measurements can be traced back to the set-up effect, where an artefact can appear based on the choice of set-up parameters (figure 4.4). Going by the location of the artefact in our data, the setpoint of $+50$ meV and a previous study of artefacts in STS data [19], we conclude that the observed artefact is indeed due to the set-up effect.

In summary, comparing our results from FT-STM measurements to previous ARPES data shows that the Fermi surface and the dispersion of the α band match well. The dispersion of the β band does not agree, the dispersion from QPI being flatter in both direction. Comparison of the self-energies yield little information, other than the rough magnitude, which agrees reasonably well.

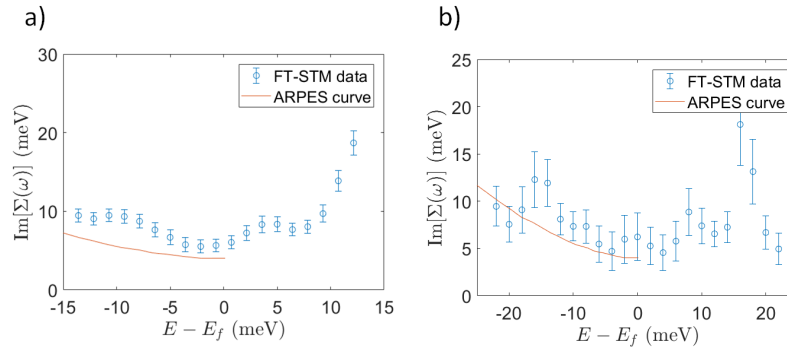


Figure 4.2: The self-energies of the β band in the ΓX direction determined by QPI data sets 1 (a) and 2 (b) plotted together with the self-energy of the α band from [5].

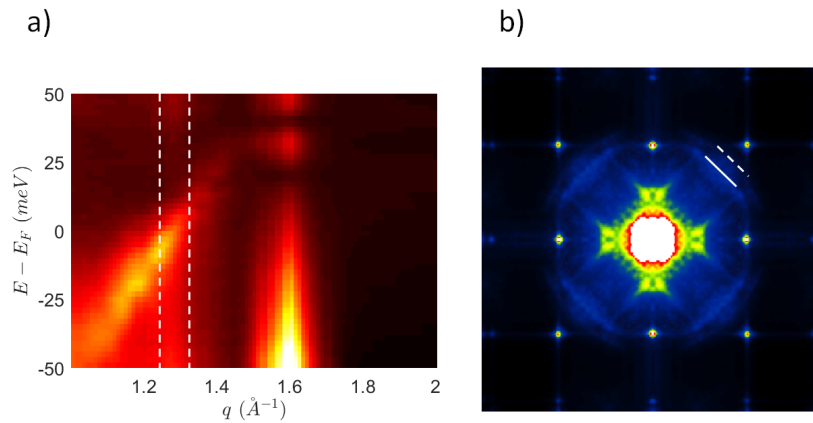


Figure 4.3: The non-dispersive artefact present in the second data set in the dispersion (left) and the constant energy layer $E = -30$ meV (right). On the left-hand side, the dashed lines indicate the momentum window where the artefact is present. On the right-hand side, the solid line indicates the β band, while the dashed line indicates the artefact.

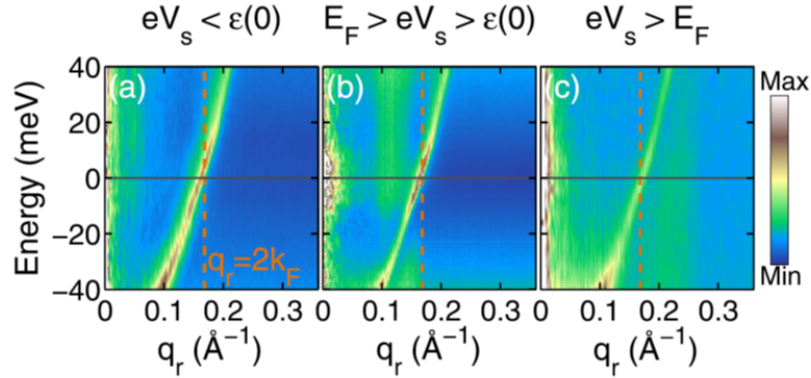


Figure 4.4: The presence of a non-dispersive artefact in STS data, and the influence of the setpoint on its location. If the set-up voltage V_s is lower than the bottom of the band $\epsilon(0)$, no artefact is present. For $eV_s > \epsilon(0)$ an artefact appears, either on the inside of the band ($V_s < 0$) or on the outside of the band ($V_s > 0$). Image from [19].

Similar conclusions were reached in previous studies comparing ARPES and FT-STM. A study on the related ruthenate Sr_2RuO_4 compares QPI data with multiple ARPES studies. The resulting comparison, shown in figure 4.5, reveals that not only the STM dispersion is flatter than the ARPES dispersion, but also a large spread in ARPES results. This large spread adds a new layer of complication to our goal of comparing STM data on Sr_2RhO_4 to ARPES since there is only one ARPES study on the rhodate which shows a dispersion. Having only one ARPES study and one QPI study, we have no way of knowing whether such a large spread in ARPES results also exists for the rhodates, whether QPI also shows such a large spread and whether the known results are on the low or high side of the spread. The same study also compares the QPI result to dHvA data. However here a discrepancy can be expected since dHvA data is averaged over k -space, while QPI and ARPES resolve k -space.

Studies on the cuprate high- T_c superconductor $\text{Bi}_2\text{Sr}_2\text{CaCu}_2\text{O}_{8+\delta}$ also reach the conclusion that the Fermi surfaces of STM and ARPES agree, the dispersions don't necessarily (figure 4.6). Also the superconducting gap reveals a discrepancy between energy scales extracted from FT-STM and photo emission. An explanation is proposed through the observation that STM only sees a smaller range of the Fermi surface which may affect the shape of the gap [3]. This is supposedly due to the fact that QPI is a 2-particle process while photo emission is a 1-particle process. While this last statement is generally true, QPI data on the ruthenates and the rhodate

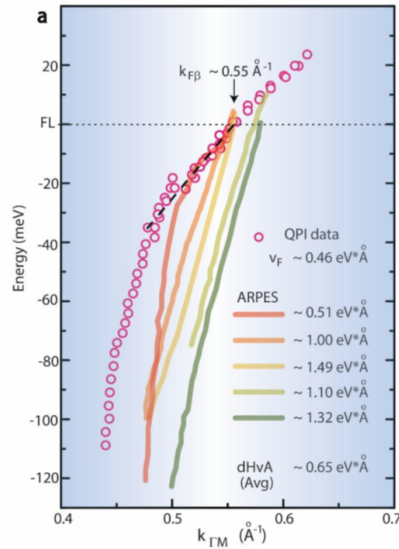


Figure 4.5: Comparison of QPI study and ARPES studies on Sr_2RuO_4 . The ARPES results are indicated by the solid lines, with the Fermi velocity next to the appropriate line. The QPI data is shown by the open circles, the low energy fit through the QPI data by the dashed black line. Also shown is the Fermi velocity obtained through dHvA data. Image from [4].

shows no sign of limited access to the Fermi surface, making this explanation specific to $\text{Bi}_2\text{Sr}_2\text{CaCu}_2\text{O}_{8+\delta}$. A study taking the reverse approach, measuring ARPES and comparing to previously published FT-STM data, shows that a discrepancy emerges when the photon polarisation used in the ARPES experiment is varied [2]. The agreement between STM and ARPES is best when the polarisation is chosen in the anti-nodal direction, as to mimic the suppression of nodal states in STM. The suppression of nodal states in STM, the same suppression mentioned in the previously mentioned study, is attributed to tunnelling through the Bi-O layer, which separates the superconducting fluid in the Cu-O layer from the sample surface. The authors also state that calculations show that this type of tunnelling elements can explain the flatter STM dispersion, however without showing or citing the calculation.

This last explanation offers a lead to explaining our results, since the Rh-O layer containing the 2D Fermi liquid is separated from the sample surface by the Sr-O cleaving plain. However at the moment it is unclear whether this can explain the discrepancies we observed.

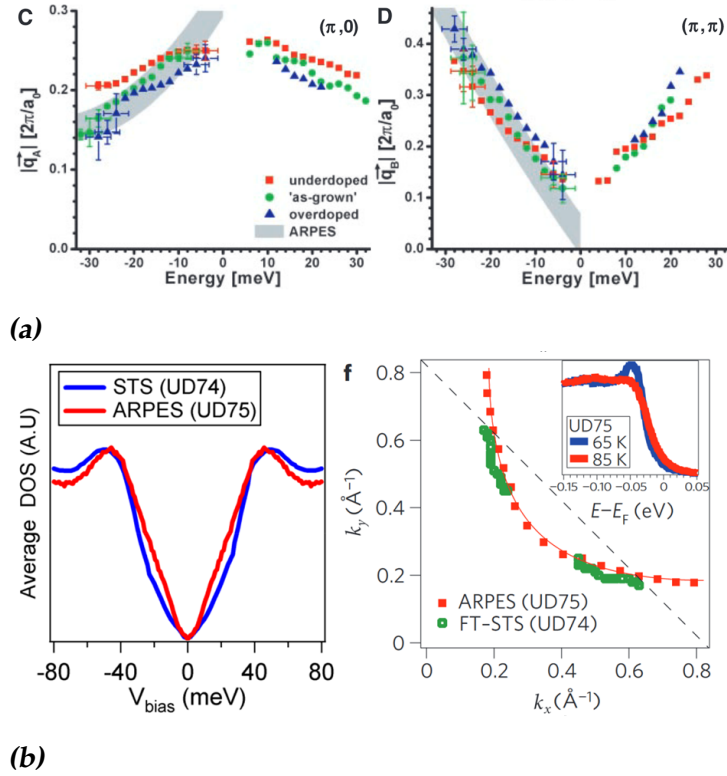


Figure 4.6: Figure 4.6a: The QPI data from a $\text{Bi}_2\text{Sr}_2\text{CaCu}_2\text{O}_{8+\delta}$ study in data symbols obtained by Hoffman et al [15] in the anti-nodal (left) and nodal direction together with contemporary ARPES results shown by the gray area. In particular the energy dependence of the scattering vector does not match well in the anti-nodal direction. Image from [15]. Figure 4.6b: The gap from STS (averaged over a field of view) and from ARPES (averaged over the Fermi surface) of $\text{Bi}_2\text{Sr}_2\text{CaCu}_2\text{O}_{8+\delta}$ (left) and the Fermi surface from both techniques (right). The gap shows a clear discrepancy between the two measurements, while the limited range of the Fermi surface for STM is clearly visible on the right-hand side. Image from [3].

Conclusion & Outlook

In this thesis we presented the bandstructure of Sr_2RhO_4 measured by STM with the goal to see how data from ARPES and FT-STM compare. To do obtain the bandstructure, we measured the local DOS over a large field of view. Oscillations in the DOS hide information on the bandstructure as they result from quasi-particle interference. Fourier transforming the DOS data yields images at constant energy of the space of scattering vectors, q -space. The bands in q -space were fitted to obtain their q -vector at $E = 0$, their dispersion and their width. From this data, with the help of a tight-binding model of Sr_2RhO_4 , the k -space bands can be reconstructed. Comparison with a previous ARPES [5, 6] study reveals that the Fermi surface agrees well between the two techniques. The dispersion from STS data is shown to be systematically flatter for one of the bands compared to ARPES results. The comparison of the self-energy is inconclusive.

Previous QPI studies in the ruthenates [4] and cuprates [2, 3, 15], and comparisons with ARPES yielded similar outcomes, with the Fermi surface agreeing well, but the dispersion proven to be more troublesome. Reaching any conclusion is further complicated by the large spread in ARPES results shown to exist in the ruthenates [4]. Nevertheless a clue is offered by a $\text{Bi}_2\text{Sr}_2\text{CaCu}_2\text{O}_{8+\delta}$ study [2] which suggests that tunnelling through a layer separating the the fluid under investigation from the sample surface may alter the dispersion found by STM. At the moment of writing no prove is shown that this explains the discrepancy between QPI and ARPES.

Further STM studies are required to solidify the discrepancies with ARPES we observed. Varying the setpoints can change whether and where artefacts are present, easing the determination of the self-energy. Using a more sophisticated model incorporating tunnelling elements to model

the Sr_2rRhO_4 bandstructure can verify whether tunnelling through the Sr-O layer causes the flattened dispersion we observe. The insights and experience gained with this study have proven useful in using QPI to study more complicated systems such as the cuprates.

Bibliography

- [1] M. F. Crommie, C. P. Lutz, and D. M. Eigler, *Imaging standing waves in a two-dimensional electron gas*, *Nature* **363**, 524 (1993).
- [2] K. McElroy, G. H. Gweon, S. Y. Zhou, J. Graf, S. Uchida, H. Eisaki, H. Takagi, T. Sasagawa, D. H. Lee, and A. Lanzara, *Elastic scattering susceptibility of the high temperature superconductor $\text{Bi}_2\text{Sr}_2\text{CaCu}_2\text{O}_{8+\delta}$: A comparison between real and momentum space photoemission spectroscopies*, *Physical Review Letters* **96**, 2 (2006).
- [3] I. M. Vishik, E. A. Nowadnick, W. S. Lee, Z. X. Shen, B. Moritz, T. P. Devereaux, K. Tanaka, T. Sasagawa, and T. Fujii, *A momentum-dependent perspective on quasiparticle interference in $\text{Bi}_2\text{Sr}_2\text{CaCu}_2\text{O}_{8+\delta}$* , *Nature Physics* **5**, 718 (2009).
- [4] Z. Wang, D. Walkup, P. Derry, T. Scaffdi, M. Rak, S. Vig, A. Kogar, I. Zeljkovic, A. Husain, L. H. Santos, Y. Wang, A. Damascelli, Y. Maeno, P. Abbamonte, E. Fradkin, and V. Madhavan, *Quasiparticle interference and strong electron-mode coupling in the quasi-one-dimensional bands of Sr_2RuO_4* , *Nature Physics* **13**, 799 (2017).
- [5] F. Baumberger, N. J. Ingle, W. Meevasana, K. M. Shen, D. H. Lu, R. S. Perry, A. P. MacKenzie, Z. Hussain, D. J. Singh, and Z. X. Shen, *Fermi surface and quasiparticle excitations of Sr_2RhO_4* , *Physical Review Letters* (2006).
- [6] R. S. Perry, F. Baumberger, L. Balicas, N. Kikugawa, N. J. C. Ingle, A. Rost, J. F. Mercure, Y. Maeno, Z. X. Shen, and A. P. Mackenzie, *Sr_2RhO_4 : a new, clean correlated electron metal*, *New Journal of Physics* **8**, 175 (2006).

-
- [7] L. J. Sandilands, W. Kyung, S. Y. Kim, J. Son, J. Kwon, T. D. Kang, Y. Yoshida, S. J. Moon, C. Kim, and T. W. Noh, *Spin-Orbit Coupling and Interband Transitions in the Optical Conductivity of Sr₂RhO₄*, *Physical Review Letters* **119**, 1 (2017).
- [8] S. J. Moon, M. W. Kim, K. W. Kim, Y. S. Lee, J. Y. Kim, J. H. Park, B. J. Kim, S. J. Oh, S. Nakatsuji, Y. Maeno, I. Nagai, S. I. Ikeda, G. Cao, and T. W. Noh, *Electronic structures of layered perovskite Sr₂ M O₄ (M=Ru, Rh, and Ir)*, *Physical Review B - Condensed Matter and Materials Physics* **74**, 5 (2006).
- [9] B. J. Kim, J. Yu, H. Koh, I. Nagai, S. I. Ikeda, S. J. Oh, and C. Kim, *Missing xy-band fermi surface in 4d transition-metal oxide Sr₂RhO₄: Effect of the octahedra rotation on the electronic structure*, *Physical Review Letters* **97**, 1 (2006).
- [10] G. Binnig, H. Rohrer, C. Gerber, and E. Weibel, *Surface studies by Scanning Tunneling Microscopy*, *Phys. Rev. Lett.* **49**, 57 (1982).
- [11] C. Chen, *Introduction to Scanning Tunneling Microscopy*, Oxford University Press, New York, 2nd edition, 2008.
- [12] J. E. Hoffman, *A Search for Alternative Electronic Order in the High Temperature Superconductor Bi₂Sr₂CaCu₂O_{8+δ} by Scanning Tunneling Microscopy*, PhD Thesis (2003).
- [13] A. R. Schmidt, *Quasiparticle Interference and the Impact of Strong Correlations on High Temperature Superconductivity*, PhD Thesis (2009).
- [14] S. Hufner, *Photoelectron Spectroscopy*, Springer-Verlag Berlin Heidelberg, third edition, 2003.
- [15] J. E. Hoffman, K. McElroy, D.-H. Lee, K. M. Lang, H. Eisaki, S. Uchida, and J. C. Davis, *Imaging Quasiparticle Interference in Bi₂Sr₂CaCu₂O_{8+δ}*, *Science* **297**, 1148 (2002).
- [16] B. Stöger, M. Hieckel, F. Mittendorfer, Z. Wang, D. Fobes, J. Peng, Z. Mao, M. Schmid, J. Redinger, and U. Diebold, *High chemical activity of a perovskite surface: Reaction of co with sr₃ru₂ o₇*, *Physical Review Letters* **113**, 1 (2014).
- [17] M. J. Lawler, K. Fujita, J. Lee, A. R. Schmidt, Y. Kohsaka, C. K. Kim, H. Eisaki, S. Uchida, J. C. Davis, J. P. Sethna, and E. A. Kim, *Intra-unit-cell electronic nematicity of the high-T_c copper-oxide pseudogap states*, *Nature* **466**, 347 (2010).

-
- [18] A. Damascelli, Z. Hussain, and Z.-X. Shen, *Angle-resolved photoemission studies of the cuprate superconductors*, *Review of Modern Physics* **75**, 473 (2003).
- [19] A. J. Macdonald, Y. S. Tremblay-Johnston, S. Grothe, S. Chi, P. Dosanjh, S. Johnston, and S. A. Burke, *Dispersing artifacts in FT-STs: A comparison of set point effects across acquisition modes*, *Nanotechnology* **27** (2016).

Appendices

Vibrations and acoustics of the UMH

A key aspect of STM is the stability of the instruments against vibrational and acoustic noise. To improve the vibrational isolation the Faculty of Science at Leiden University has constructed a new measurement hall called the Ultra Microscopy Hall or UMH. The UMH features 16 measurement islands which are isolated from vibrations by airsprings on the corners of each islands. These islands were designed to have a much better vibrational isolation than the current location of the STM set-up, being the Kamerlingh Onnes Laboratory (KOL) at the Leiden University.

To verify this statement and to benchmark the performance of the new islands, the vibrations were measured at both locations using a Guralp 40T. To aid in tracking the origin of noise peaks, the acoustics of the UMH were measured using a G.R.A.S. 46AF microphone. The results of these measurements are presented below.

The legs of the airsprings are placed in the basement of the UMH (see figure A.1). On top of the airsprings is a 3×3 m concrete block which forms the island. The islands are accessible from the ground level by holes in the concrete walking floor through which the islands point. The surface of the islands is roughly 50 cm below the ground level floor. A floating floor can be placed over the island to cover the hole without making contact between the island and the ground level floor. Vibrations were measured on the UMH basement and on the island surface.

In our vibration measurements, a sampling frequency on 250 Hz was used and the data was stored in files containing one minute of measurements. Each file is split up into groups of 600 points with an overlap of 50%. Each group is weighted with a Hanning window before taking the

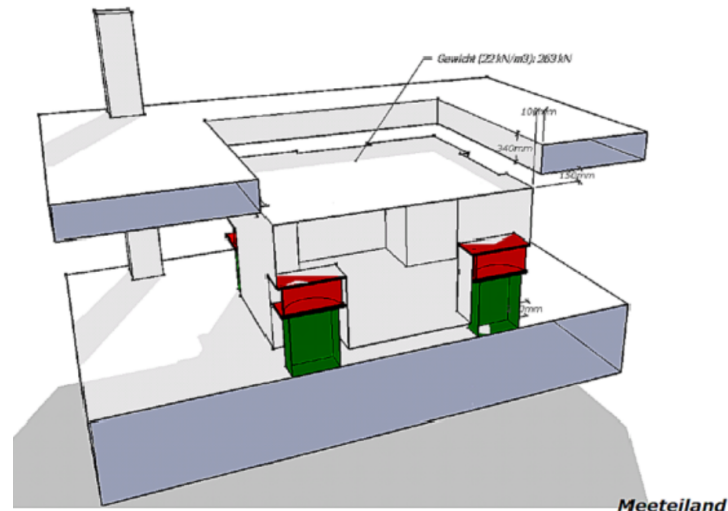


Figure A.1: Drawing of an island in the UMH. The legs of the airsprings are shown in green, the airsprings themselves in red. A floating floor can be installed to cover the hole in the ground level floor.

Fourier transform. The Fourier transforms of each group is then averaged to obtain the Fourier transform of the full datafile. This way of taking Fourier transforms is called the Welch algorithm and has the advantage of reducing noise in final spectrum. In this way, the frequency resolution is determined by size of the grouping.

The acoustics measurements were performed using a sample frequency of 1650 Hz. Here too the welch algorithm was used to do the analysis, but now with groups containing 5000 points.

A comparison of the vibrations in the old location (KOL) and the new location (UMH) is shown in figure A.2. Here, KOL pit indicates the place where the legs of the STM set-up currently stand. UMH island 30f is one of the islands where an STM is planned to go. The measurement on the island surface was taken with the floating floor in place. The substantial better noise level on the UMH island is clear, especially for the low frequencies.

To track the evolution of noise peaks and with the aim to correlate peaks in the vibration spectrum with acoustics noise, vibrational and acoustic spectra were measured on two different islands in the UMH, one of which had the legs under the airsprings raised. The 30 minute average spectra (figure A.3) show three major peaks that seem to be tied to acoustics: 29, 49, 100 Hz. To check this, the intensity of these frequencies were track over a prolonged period of time (figure A.4). The data from the

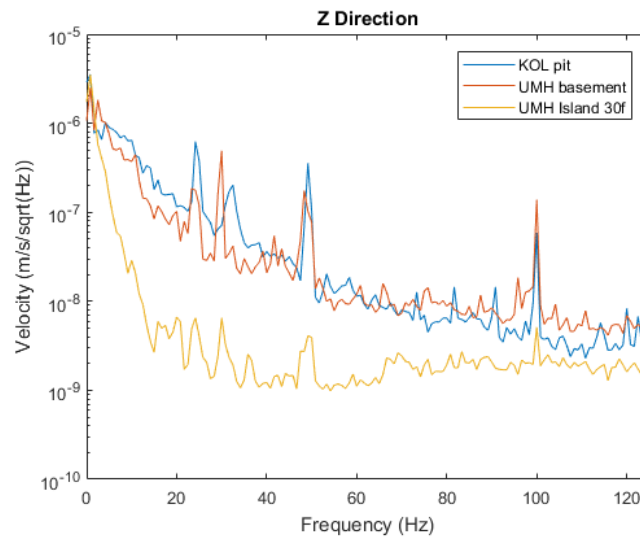


Figure A.2: Vibrational spectra in the vertical direction at the current location of the STM (KOL pit), the basement of the UMH (UMH basement) and on one of the islands in the UMH (UMH island 30f).

25 – 30 Hz indicate that the 29 Hz peaks in the vibrations and acoustics are not related, since the variations in intensity for both peaks do not follow each other. The data from the 45 – 50 Hz band shows only white noise with no changes in time, making the data inconclusive. The band centred around 100 Hz do show some correlation between vibration and acoustics, but only for one of the islands, the other island showing no such correlation. As a result here too it is hard to make a statement about the relation between vibration and acoustics. We do find correlation between vibrations and acoustics in the 20 – 25 Hz band on both islands. This leads us to believe that the vibrations in this band have an acoustic origin. At the time of the measurements the UMH was not in use yet, except for some water coolers. These are situated closer to the raised island than to the standard, non-raised island. This is reflected in the noise level in the 20 – 25 Hz band in the averaged spectra, being a bit higher for the raised island, suggesting that this noise can be related to the water coolers.

To check the performance of several islands and the difference in performance between them, vibration spectra in three different directions X,Y,Z were measured on five different islands, one of which was the raised island, and with the floating floor in place for some of them. The results (figure A.5) indicate that there is a difference between the island. However, based on the same data we note that the differences cannot be traced

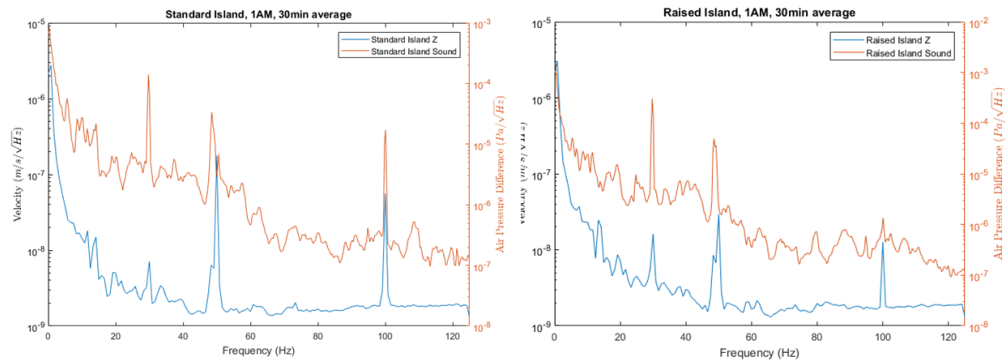


Figure A.3: 30 minute average of the vibration (blue) and acoustic (red) spectrum on two of the islands in the UMH. The spectra were taken at 1AM to eliminate noise generated by people and traffic as much as possible. On the left are the spectra from an island as it was originally designed, on the right are the spectra from an island where the legs under the airsprings were raised using a stack of tiles and rubber mats.

to either the floating floor being in place or the island being raised. Rather, it seems that the differences are intrinsic to the islands themselves.

We conclude that the UMH islands provide a significantly better vibration isolation compared to the KOL. Vibration measurements across multiple islands suggest that the presence of a floating floor above the island surface and elevating the legs of the airsprings does not hinder the performance, and that differences between the islands are inherent to the islands. Based on the time dependence of both the vibrational and acoustic noise, the noise peak around 25 Hz seems to have an acoustic origin, possibly related to the presence of water coolers in one of the corridors of the hall.

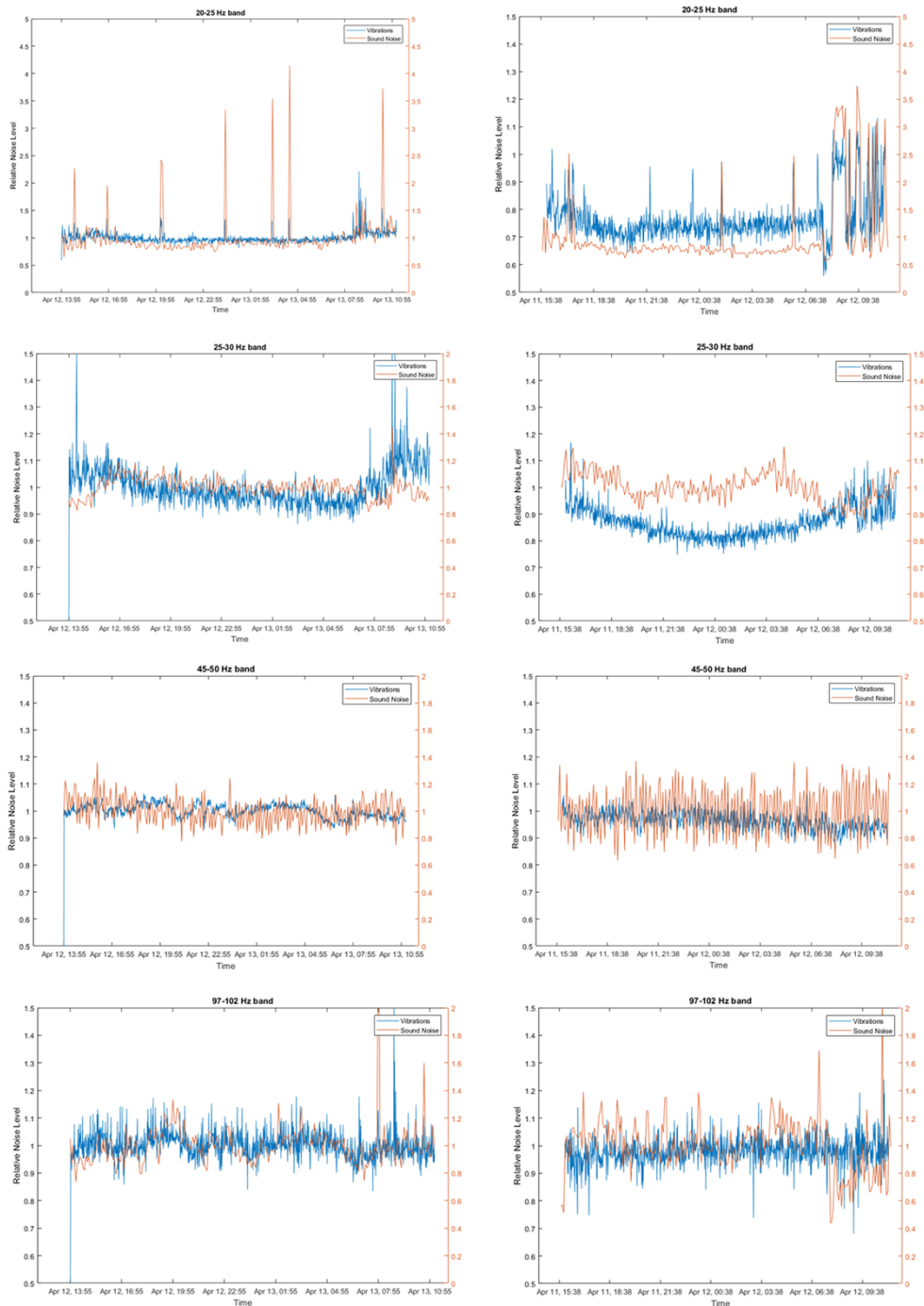


Figure A.4: Time dependence of the vibrational and acoustic noise in various frequency bands (top to bottom: 20 – 25 Hz, 25 – 30 Hz, 45 – 50 Hz, 97 – 102 Hz). The left-hand column shows the noise on a standard island, the right-hand column the noise on the raised island.

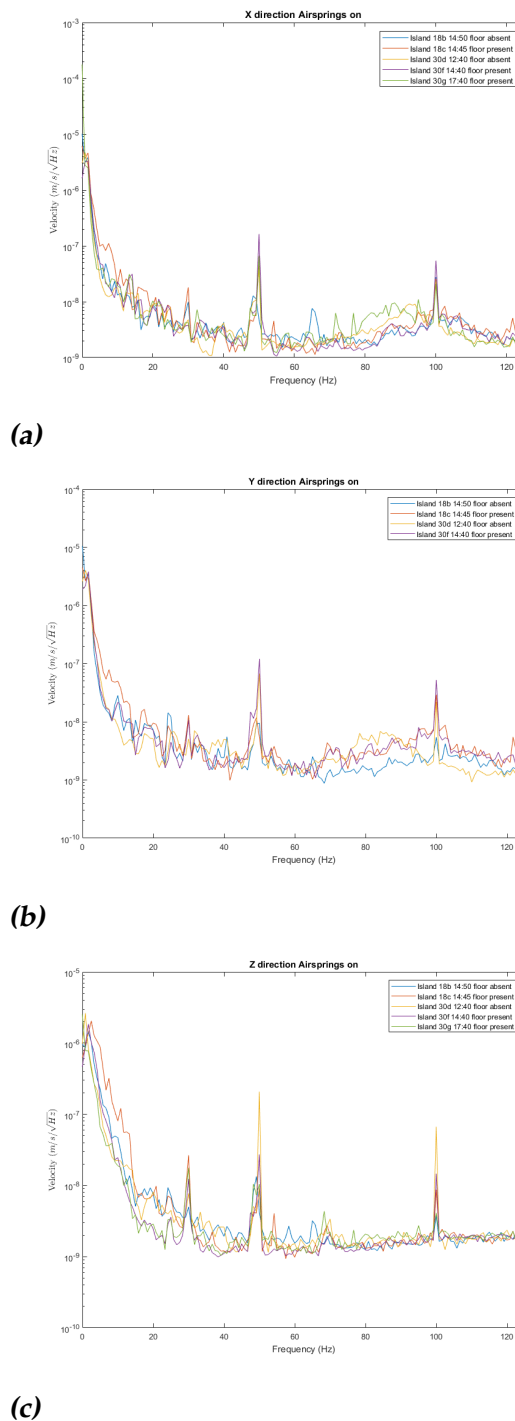


Figure A.5: Vibration spectra on different islands in the UMH in different directions at various times of the day. Island 18b is referred to in the main text as the raised island. The spectrum in the Y direction for island 30g due to faulty data storage.